Standing wave hard x-ray photoemission study of the structure of the interfaces in Ta/Co_2FeAl/MgO multilayer

Pramod Vishwakarma[1], Maheswar Nayak[2], V. R. Reddy[3], Andrei Gloskovskii[4], Wolfgang Drube[4], and Ajay Gupta[5,*]

[1] *Amity Center for Spintronic Materials, Amity University UP, Sector 125, Noida 201 313, India*

[2] *Raja Ramanna Centre for Advanced Technology, Indore 452 013, India*

[3] *UGC-DAE Consortium for Scientific Research, University Campus, Khandwa Road, Indore 452 001, India*

[4] *Deutsches Elektronen-Synchrotron DESY, Notkestraße 85, 22607 Hamburg, Germany*

[5] *Department of Physics, University of Petroleum and Energy Studies, Bidholi Campus, Dehradun 248007, India*

**Corresponding author: e-mail: ajay.gupta@ddn.upes.ac.in*

ABSTRACT

Interfaces of the magnetic layer in the heterostructure Ta/Co_2FeAl/MgO have been studied using hard x-ray photoelectron spectroscopy (HAXPES). Depth-selective information with sub-nanometer resolution is obtained using x-ray standing waves. It is found that the two magnetic species namely, Co and Fe behave very differently at the interfaces; 54% of Fe in the magnetic layer gets either oxidised or alloyed with Ta at the interfaces, as against 48% of Co. Oxidation state of both Co and Fe decreases, as one moves away from the MgO interface. On the average about 0.36 nm of Co_2FeAl gets oxidised at MgO interface and 0.66 nm gets alloyed with Ta at the bottom interface. Thermal annealing at 200℃ results in further oxidation of Fe, accompanied by a partial reduction of Co. It is suggested that this opposite behaviour of Fe and Co at the

MgO interface may be the cause of the thermal annealing induced shift of the centroid of Fe distribution towards MgO layer, as observed in some STEM studies in such heterostructures.

KEYWORDS. Spintronics; Ta/CFA/MgO heterostructure; Interfaces; Hard x-ray photoelectron spectroscopy; X-ray standing waves; Thermal annealing

1. INTRODUCTION

Key challenges in the spintronics research are to achieve low power consumption, faster information processing, and higher density data storage in the ultrathin film based magnetic memory devices. Consequently, ultrathin film systems incorporating ferromagnet (FM) and heavy metal (HM) layer interfaces are gaining extensive attention in the field of spintronic. These structures give rise to various novel mechanisms and phenomena, relevant for the emergent field of spintronics such as, spin Hall and inverse spin Hall effects[1-4], interfacial Rashba effect [5-8], spin-orbit torque (SOT) [9-11], and interfacial Dzyaloshinskii-Moriya interaction (IDMI) [12-15]. It was shown that strong spin-orbit coupling (SOC) in heavy metals like W, Ta, Hf, Pt results in 'spin-orbit torque' on adjacent FM layer and can be used to control the magnetization of FM layer by passing a current in HM layer [5, 10, 16, 17]. SOC also underlies the interfacial Dzyaloshinskii-Moriya interaction which can influence the domain wall spin structure and thus its current-driven dynamics [18-20]. All these phenomena are highly sensitive to the interfacial structure.

Heusler alloys are attractive candidates as FM electrode for spintronic applications due to their high Curie temperatures, tunable electronic properties and very high spin polarization at room temperature [21-23]. Among these Heusler alloys, Co_2FeAl (CFA) has gained special attention due to very low Gilbert damping constant and large magnetic moment [24-26]. It is

also reported that magnetic tunnel junction (MTJ) with CFA shows very high tunnel magneto resistance (TMR) at room temperature [27]. Extensive studies have been done in the literature as a function of layer compositions and structure as well as post-deposition annealing treatment, in order to optimize the magnetic anisotropy energy, SOT and IDMI. However, the underlying mechanism responsible for the observed variations in perpendicular magnetic anisotropy PMA, SOT or IDMI is still not clear. Since all these phenomena are predominantly interfacial in origin [28-34], a detailed understanding of the structure of the interfaces in these systems will be valuable in understanding the underlying mechanisms, which is important for future spintronic applications.

In the present work, we study the interfaces in Ta/CFA/MgO heterostructure, and evolution of the same with thermal annealing, using hard x-ray photoemission (HAXPES). Measurements were performed under x-ray standing wave (XSW) condition in order to achieve sensitivity of the technique to the interfaces. Depth-resolved information helps in assigning specific peaks in HAXPES to interfacial alloy. Depth variation of the oxidation state of the two magnetic species has also been elucidated. Present results show that Fe and Co behave very differently at the interfaces.

2. EXPERIMENTAL

Multilayer having a nominal structure: MgO (4 nm)/Ta (6.7 nm)/CFA (1.4 nm)/MgO (0.65 nm)/Ta (1.2 nm) was deposited simultaneously on Si/[Mo (2.6 nm)/Si (4.1 nm)]$_{x18}$ multilayer as well as on a Si (100) substrate. Deposition was done using ion beam sputtering in a vacuum chamber with a base pressure of $2x10^{-8}$ mbar. A broad beam ion source model Kauffman and Robinson KDC 10 was used to generate 600 eV Ar^{+} ions to sputter the targets.

The Mo/Si multilayer was used for x-ray standing wave (XSW) formation and was prepared at Synchrotron Utilization Section, RRCAT, Indore using magnetron sputtering. A schematic diagram of the sample structure is shown in the Figure 1. X-ray reflectivity measurements were done using Bruker D8 diffractometer fitted with a Göbel mirror on the incident beam side in order to obtain a parallel monochromatic beam of Cu K_α radiation. To get information about the electronic structure of the interfaces hard x-ray photoemission measurements were done at P09 beamline in PETRA III synchrotron radiation source, Hamburg [35, 36], using x-ray energy of 5945 eV. Sample was mounted vertically on Omicron manipulator having a rotation stage with an angular resolution of 0.002°. The x-ray beam, linearly polarized in horizontal plane, was allowed to fall on the sample at a grazing incidence. The angle between the x-ray propagation direction and the analyser was 90°. Since the angle of incidence of x-rays with respect to the surface of the sample was around 1° or less, the takeoff angle was almost 90°. To enhance the sensitivity of the technique to the interfaces, measurements were performed under x-ray standing wave condition. Thermal annealing of the multilayer sample was done at 200℃ for 1h in a vacuum of $1X10^{-6}$ mbar.

3. RESULTS

Figure 2 gives the x-ray reflectivity of (a) the Mo/Si multilayer before the deposition of the structure to be studied, (b) MgO/Ta/CFA/MgO/Ta deposited on the Si substrate and (c) the complete multilayer sample. All the three reflectivity patterns were fitted using Parratt's formulism taking the thicknesses as well as the roughnesses of different layers as fitting parameters. The fittings of the reflectivities of bare Mo/Si multilayer and the MgO/Ta/CFA/MgO/Ta structure gave the values of the individual layer thicknesses and roughnesses, which were then used to fit the reflectivity of the complete multilayer sample. The

results of fitting are summarized in Table I. It may be noted that, in the reflectivity of the complete multilayer structure, strong features of the underlying Mo/Si multilayer tend to obscure the modulations due to the MgO/Ta/CFA/MgO/Ta structure, thus making it difficult to extract reliable information about its structure. An independent analysis of the reflectivity of the bare Mo/Si multilayer and the MgO/Ta/CFA/MgO/Ta structure helped in precise determination of the structure of the complete multilayer sample.

Precise structure of the multilayer as obtained from the fittings of the reflectivity patterns was used to simulate the depth dependent x-ray intensity inside the multilayer as a function of the grazing angle of incidence of x-rays, and is shown in Figure 3 (a). Parratt's recursive formalism was used to calculate the x-ray intensity as a function of depth in the multilayer [37]. Taking the complex index of refraction of the j^{th} layer as $n_j = 1- \delta_j + i\beta_j$, reflected and transmitted amplitudes at each interface have been calculated. Different amplitudes are added coherently, square of which give the x-ray intensity at a given point. One can see that, two types of x-ray standing waves are formed in the sample: i) up to the critical angle for total reflection of x-rays from Ta, defined as $\theta_c = \sqrt{(2\delta_{Ta})}$, standing waves are formed due to interference of the incident wavefront with the wavefront totally reflected from the surface of the bottom Ta layer [38] . With increasing angle of incidence, the nodes and antinodes of the standing wave shift downward, making it possible to achieve depth-selectivity by doing measurements at different angles of incidence. ii) Second standing wave pattern is formed in the angular range from 0.85° to 1.1°, spanning the first Bragg peak of Mo/Si multilayer [39]. At the Bragg condition, reflected amplitudes from different interfaces in Mo/Si multilayer are in phase and add up coherently to build up a strong reflected wavefront. Standing waves are formed due to interference between the incident and reflected wavefronts. One can see that for both types of standing waves, the

positions of various antinodes move along the depth with varying incident angle. Accordingly, four angles (0.63°, 0.73°, 0.82° and 1.02°) were selected in order to get preferential information about MgO/CFA interface, bulk of CFA layer and CFA/Ta interface. Figure 3 (b), gives the simulated depth variation of x-ray intensity for these four angles. One can see that for 0.63° and 1.02°, the x-ray intensity has a steep gradient across the CFA layer, with intensity significantly higher at MgO/CFA interface, while for 0.82°, the slope is reverse and the x-ray intensity is significantly higher at CFA/Ta interface. For 0.73°, x-ray intensity across the CFA layer is almost constant. HAXPES measurements were done at these angles of x-ray incidence. Since for each of these angles of incidence the two interfaces MgO/CFA, CFA/Ta and bulk of CFA are weighted differently, a comparison of four XPS spectra helped to identify the origin of different features in the photoelectron spectra, and also to get depth-selective information.

Figure 4, gives the $2p_{3/2}$ spectra of Fe taken at these four angles of incidence. Spectra were fitted with five overlapping peaks centred at 707.0 eV, 707.9 eV, 709.0 eV, 710.0 eV and 711.3 eV respectively. The energies of the peaks at 709.0 eV, 710.0 eV and 711.3 eV were taken from the literature on oxides of Fe [40-45]. Results of fitting are summarized in Table 2. The peak at 707.0 eV corresponds to the metallic Fe in CFA [40, 41]. The three peaks in the energy range from 709 to 711.3 eV are identified with various oxides of iron; While peaks at 709.0 eV and 711.3 eV correspond to Fe^{2+} and Fe^{3+} states respectively [42], peak at 710 eV may correspond to either Fe^{2+} or Fe^{3+} state [41, 44, 45]. The peak at 707.9 eV which could not be identified with any known compound of Fe, most likely corresponds to interfacial alloying at CFA/Ta interface. It may further be noted that, in some studies of Fe/Pd and Fe/Pt system a peak in the XPS pattern shifted from that of Fe metal by ~1 eV on the higher binding energy side, has

been attributed to alloy of Fe with the heavy metal [46]. This gives additional support to our conjecture that the peak at 707.9 eV corresponds to the Fe-Ta alloy at the interface.

In order to further confirm the origin of the peak at 707.9 eV, we took recourse to the incident angle dependence of the relative intensities of different peaks. As seen from Figure 3, the spectra corresponding to angle of incidence 0.63° and 1.02° have higher weightage for the MgO/CFA interface, while that corresponding to 0.82° has higher weightage of the CFA/Ta interface, and the one corresponding to 0.73° has constant weightage across the CFA layer. Figure 5 gives the relative intensities of the peaks at 707 eV, 707.9 eV and the sum of the intensities of the three peaks in the energy range 709 to 711.3 eV for these four angles of incidence. One can see that the peak at 707.9 eV has higher intensity for the angle of incidence α = 0.82° for which antinode of XSW is closer to the CFA/Ta interface, and its intensity decreases as the antinode moves to the center of CFA layer (α = 0.73°) and then to the MgO/CFA interface (α = 0.63°, 1.02°). On the other hand, sum of the intensities of the three peaks in the energy range 709 eV to 711.3 eV, which correspond to the oxide phases, has the opposite behaviour. This confirms the assignment of different peaks to MgO/CFA and CFA/Ta interfaces. For angle of incidence of 0.73°, the x-ray intensity is almost constant across the thickness of CFA layer. Therefore, the relative intensities of the three sets of peaks at this angle can be used to get the fraction of iron atoms at the two interfaces and in the bulks of the CFA layer. However, it may be noted that, the photoelectrons emitted from different regions of the CFA layer will get attenuated differently due to self absorption in the CFA layer, and the correction for the same should be applied in order to correlate the intensity of a peak with the thickness of the corresponding region. Following relations are derived for the intensities of the peaks corresponding to the three regions of the CFA layer:

$$I_t = A\lambda\left[1 - e^{-d_t/\lambda}\right], \quad \ldots(1)$$

$$I_m = A\lambda e^{-D/\lambda}\left[e^{(D-d_t)/\lambda} - e^{d_b/\lambda}\right], \quad \ldots(2)$$

$$I_b = A\lambda e^{-D/\lambda}\left[e^{d_b/\lambda} - 1\right], \quad \ldots(3)$$

where I_t, I_m, and I_b are respectively the intensities of the peaks corresponding to the top interface (oxide), middle region of the layer (CFA) and the bottom interface (CFA-Ta alloy), D is the total thickness of the CFA layer, d_t and d_b are the thicknesses of the top interface and bottom interface, and λ is the inelastic mean free path of the photoelectrons in CFA layer. A is a factor which takes care of the photoelectric cross section and the number density of absorbing atoms. Taking the literature values of λ = 6.0 nm for 5 keV photoelectrons in Fe [47], and the relative intensities of the peaks corresponding to Fe-oxide, Fe in CFA and Fe-Ta alloy from Table II (23%, 46% and 31% respectively), one finds that ~ 20% of iron atoms get oxidized at MgO/CFA interface, while 34% of iron gets intermixed with Ta.

Figure 6, gives the $2p_{3/2}$ spectra of Co corresponding to the above four angles of incidence. XPS spectra of Co were fitted with six peaks. The peak at 778.3 eV corresponds to metallic Co in CFA [48, 49], the peaks at energies 779.6 eV and 780.5 eV correspond to Co^{3+} and Co^{2+} states in the oxide phases [50]. The peak at 779 eV may be assigned to CFA/Ta interface, in conformity with some studies in Co/Pt system in which alloy of Co with the heavy metal has been found to have peak at binding energy of 0.6 eV higher than that of Co metal [51, 52]. Peaks at 782 eV and 783.5 eV are the satellite or Plasmon peaks [53]. Results of fitting are summarized in Table II. Figure 7, gives the relative intensities of the oxide, metallic Co and Co-Ta alloy components corresponding to different angles of incidence. Increase in the intensity of the peak at 779 eV as a function of depth further supports the assignment of this peak to Co-Ta alloy. Variation of oxide phase as a function of depth, if any, is within experimental errors.

From the analysis of the spectrum at 0.73° angle of incidence, one finds that the fraction of Co atoms in oxide phase, metallic CFA and Co-Ta alloy phase are 16%, 52% and 32% respectively.

Figures 8 and 9, give the $Fe2p_{3/2}$ and $Co2p_{3/2}$ spectra of the multilayer annealed at 200℃ for 1h. The spectra were fitted in the same manner as those for pristine sample, and the results of fitting are summarized in Table III. Figures 10 and 11, give the depth dependence of various components of the spectra. One can see that after annealing there is an observable increase in the intensities of the peaks corresponding to the iron oxides while those of cobalt oxides decrease.

4. DISCUSSION

From Table II one finds that, at the interface between MgO/CFA, Fe is present in both 2+ and 3+ states. Further, as one moves away from MgO/CFA interface, the area under the peaks at 710 eV and 711.3 eV decreases significantly while that under the peak at 709 eV remains almost constant. This suggests that as one moves away from the MgO/CFA interface the average oxidation state of iron decreases. From the analysis in the previous section, one can see that, 20% of Fe is oxidized at MgO/CFA interface, while 34% of it is alloyed at CFA/Ta interface, while in the case of Co, 16% of it is oxidized at MgO/CFA interface, and 32% is alloyed with Ta at CFA/Ta interface. Thus, in the as-deposited multilayer, Fe preferentially gets mixed at both the interface. Further, as the angle of incidence is varied, there is only a small variation in the intensities of various peaks of Co, as compared to the observed behavior of various peaks in the case of Fe. The implications of this can be understood as follows. For a given x-ray intensity gradient across the CFA layer, the difference in the weight factor of the two interfaces will be higher, higher the width of the depth-distribution of Fe or Co. This suggests that Fe atoms diffuse deeper inside the MgO and Ta layers making the depth distribution of the Fe atoms much wider as compared to that of Co atoms.

As shown in Table III, after annealing at 200℃ there is significant redistribution of intensities under different peaks. Following the arguments similar to those in the case of pristine multilayer, following inference can be drawn: a) Annealing results in further oxidation of Fe at MgO/CFA interface taking the fraction of oxidised Fe atoms from 20% to 26%. Also, the average oxidation states of Fe increases. On the other hand at CFA/Ta interface, alloying of Fe decreases. b) In contrast to Fe, the fraction of oxidized Co atoms decreases substantially after annealing.

Since after annealing Fe concentration at the MgO/CFA interface becomes substantially higher than that of Co, centroid of the Fe profile would be shifted towards MgO layer relative to that of Co. In this context it is interesting to note that in a recent cross-sectional STEM study of Cr/Co_2FeAl/MgO system, it was found that after annealing at 350℃ the centroid of the concentration profile of Fe gets shifted towards MgO layer by about 0.1 nm [54]. Present results are in conformity with this behavior, and suggest that preferential oxidation of Fe at the interface with MgO is the cause of such shift. Furthermore, in the present case, since x-ray measurements are done non-destructively on the same area of the sample before and after annealing, the results are more reliable.

5. CONCLUSIONS

In conclusion, structure of the interfaces of Co_2FeAl in a Ta/Co_2FeAl/ MgO trilayer have been studied using hard x-ray photoelectron spectroscopy. Depth selectivity in the measurements has been achieved using x-ray standing waves. Variation in the intensities of various peaks in HAXPES spectra as a function of depth helps in getting exclusive information about the two interfaces. It is found that on the average about 0.36 nm of the magnetic layer gets oxidized at

the interface with MgO, while at the interface with Ta, 0.66 nm of CFA gets alloyed with Ta. Oxidation state of both Fe and Co decreases as one moves away from the MgO interface. Further, Fe exhibits higher diffusion at the two interfaces as compared to Co. Thermal annealing at 200℃ for 1h results in further oxidation of Fe and at the same time partial reduction of Co. Preferential diffusion of Fe at the MgO interface would cause a shift of the concentration profile of Fe towards MgO interface, relative to Co. Present results are in conformity with some STEM observations in Cr/Co_2FeAl/Ta, in which Fe concentration profile was found to be shifted towards MgO by ~0.1 nm relative to Co, and suggest that preferential affinity of Fe towards oxygen is the cause of such shift. It may be noted that, in the present case, since x-ray measurements are done non-destructively on the same part of the sample before and after annealing, the results are more reliable.

ACKNOWLEDGMENTS

Thanks are due to Anil Gome for help in XRR measurements. Pramod Vishwakarma is project associate supported by UGC-DAE, CSR, Indore. Funding for the HAXPES instrument at beamline P09 by the Federal Ministry of Education and Research (BMBF) under contracts 05KS7UM1 and 05K10UMA with Universität Mainz; 05KS7WW3, 05K10WW1 and 05K13WW1 with Universität Würzburg is gratefully acknowledged. Support for the experiment at PETRA-III, Germany, was provided by the Department of Science and Technology, Government of India through Jawaharlal Nehru Centre for Advanced Scientific Research.

REFERENCES

[1] Pai, C.F.; Liu, L.; Li, Y.; Tseng, H.W.; Ralph, D.C.; Buhrman, R.A. Spin transfer torque devices utilizing the giant spin Hall effect of tungsten. Appl. Phys. Lett. 2012, 101(12), 122404.

[2] Seki, T.; Hasegawa, Y.; Mitani, S.; Takahashi, S.; Imamura, H.; Maekawa, S.; Nitta, J; Takanashi, K. Giant spin Hall effect in perpendicularly spin-polarized FePt/Au devices. Nat. Mater. 2008, 7(2), 125-129.

[3] Jungwirth, T.; Wunderlich, J.; Olejník, K. Spin Hall effect devices. Nat. Mater. 2012, 11(5), 382-390.

[4] Ando, K.; Takahashi, S.; Ieda, J.; Kajiwara, Y.; Nakayama, H.; Yoshino, T.; Harii, K.; Fujikawa, Y.; Matsuo, M.; Maekawa, S.; Saitoh, E. Inverse spin-Hall effect induced by spin pumping in metallic system. J. Appl. Phys. 2011, 109(10), 103913.

[5] Miron, I.M.; Gaudin, G.; Auffret, S.; Rodmacq, B.; Schuhl, A.; Pizzini, S.; Vogel, J.; Gambardella, P. Current-driven spin torque induced by the Rashba effect in a ferromagnetic metal layer. Nat. Mater. 2010, 9(3), 230-234.

[6] Pi, U. H.; Kim, K. W.; Bae, J. Y.; Lee, S. C.; Cho, Y. J.; Kim, K. S.; Seo, S. Tilting of the spin orientation induced by Rashba effect in ferromagnetic metal layer. Appl. Phys. Lett. 2010, 97, 162507.

[7] Miron, I.M.; Garello, K.; Gaudin, G.; Zermatten, P.J.; Costache, M.V.; Auffret, S.; Bandiera, S.; Rodmacq, B.; Schuhl, A.; Gambardella, P. Perpendicular switching of a single ferromagnetic layer induced by in-plane current injection. Nature 2011, 476(7359), 189-193.

[8] Wang, X.; Manchon, A. Diffusive spin dynamics in ferromagnetic thin films with a Rashba interaction. Phys. Rev. Lett., 2012,108(11), 117201.

[9] Woo, S.; Mann, M.; Tan, A.J.; Caretta, L.; Beach, G.S. Enhanced spin-orbit torques in Pt/Co/Ta heterostructures. Appl. Phys. Lett. 2014, 105(21), 212404.

[10] Liu, L.; Pai, C.F.; Li, Y.; Tseng, H.W.; Ralph, D.C.; Buhrman, R.A. Spin-torque switching with the giant spin Hall effect of tantalum. Science 2012, 336(6081), 555-558.

[11] Liu, L.; Lee, O.J.; Gudmundsen, T.J.; Ralph, D.C.; Buhrman, R.A. Current-induced switching of perpendicularly magnetized magnetic layers using spin torque from the spin Hall effect. Phys. Rev. Lett. 2012, 109(9), 096602.

[12] Kim, N.H.; Jung, J.; Cho, J.; Han, D.S.; Yin, Y.; Kim, J.S.; Swagten, H.J.; You, C.Y. Interfacial Dzyaloshinskii-Moriya interaction, surface anisotropy energy, and spin pumping at spin orbit coupled Ir/Co interface. Appl. Phys. Lett. 2016, 108(14), 142406.

[13] Ma, X.; Yu, G.; Tang, C.; Li, X.; He, C.; Shi, J.; Wang, K.L.; Li, X.,. Interfacial Dzyaloshinskii-Moriya Interaction: Effect of 5 d Band Filling and Correlation with Spin Mixing Conductance. Phys. Rev. Lett. 2018,120(15),157204.

[14] Torrejon, J.; Kim, J.; Sinha, J.; Mitani, S.; Hayashi, M.; Yamanouchi, M.; Ohno, H. Interface control of the magnetic chirality in CoFeB/MgO heterostructures with heavy-metal underlayers. Nat. Commun. 2014, 5(1), 1-8.

[15] Yang, H.; Thiaville, A.; Rohart, S.; Fert, A.; Chshiev, M. Anatomy of dzyaloshinskii-moriya interaction at Co/Pt interfaces. Phys. Rev. Lett. 2015, 115(26), 267210.

[16] Ando, K.; Takahashi, S.; Harii, K.; Sasage, K.; Ieda, J.; Maekawa, S.; Saitoh, E. Electric manipulation of spin relaxation using the spin Hall effect. Phys. Rev. Lett. 2008, 101(3), 036601.

[17] Manchon, A.; Zhang, S. Theory of spin torque due to spin-orbit coupling. Phys. Rev. B 2009, 79(9), 094422.

[18] Emori, S.; Bauer, U.; Ahn, S.M.; Martinez, E.; Beach, G.S. Current-driven dynamics of chiral ferromagnetic domain walls. Nat. Mater. 2013, 12(7), 611-616.

[19] Kim, K.W.; Lee, H.W.; Lee, K.J.; Stiles, M.D. Chirality from interfacial spin-orbit coupling effects in magnetic bilayers. Phys. Rev. Lett. 2013, 111(21), 216601.

[20] Sampaio, J.; Cros, V.; Rohart, S.; Thiaville, A.; Fert, A. Nucleation, stability and current-induced motion of isolated magnetic skyrmions in nanostructures. Nat. Nanotech. 2013, 8(11), 839-844.

[21] Galanakis, I.; Dederichs, P.H. eds. Half-metallic alloys: fundamentals and applications. Berlin: Springer, 2005, 676, 1-39.

[22] Hirohata, A.; Kikuchi, M.; Tezuka, N.; Inomata, K.; Claydon, J.S.; Xu, Y.B.; Van der Laan, G. Heusler alloy/semiconductor hybrid structures. Current Opinion Solid State Mater. Sci. 2006, 10(2), 93-107.

[23] De Groot, R.A.; Mueller, F.M.; Van Engen, P.G.; Buschow, K.H.J. New class of materials: half-metallic ferromagnets. Phys. Rev. Lett. 1983, 50(25), 2024.

[24] Elmers, H.J.; Wurmehl, S.; Fecher, G.H.; Jakob, G.; Felser, C.; Schönhense, G.; Field dependence of orbital magnetic moments in the Heusler compounds Co_2FeAl and $Co_2Cr_{0.6}Fe_{0.4}Al$. Appl.Phys. A 2004, 79(3), 557-563.

[25] Qiao, S.; Nie, S.; Zhao, J.; Huo, Y.; Wu, Y.; Zhang, X. Magnetic and Gilbert damping properties of L_{21}-Co_2FeAl film grown by molecular beam epitaxy. Appl. Phys. Lett. 2013, 103(15), 152402.

[26] Belmeguenai, M.; Tuzcuoglu, H.; Gabor, M.S.; Petrisor Jr, T.; Tiusan, C.; Berling, D.; Zighem, F.; Chauveau, T.; Chérif, S.M.; Moch, P. Co_2FeAl thin films grown on MgO substrates: Correlation between static, dynamic, and structural properties. Phys. Rev. B 2013, 87, 184431.

[27] Wang, W.; Liu, E.; Kodzuka, M.; Sukegawa, H.; Wojcik, M.; Jedryka, E.; Wu, G.H.; Inomata, K.; Mitani, S.; Hono, K. Coherent tunneling and giant tunneling magnetoresistance in Co_2FeAl/MgO/CoFe magnetic tunneling junctions. Phys. Rev. B 2010, 81(14), 140402.

[28] Peng, S.; Zhu, D.; Zhou, J.; Zhang, B.; Cao, A.; Wang, M.; Cai, W.; Cao, K.; Zhao, W. Modulation of heavy metal/ferromagnetic metal interface for high-performance spintronic devices. Adv. Electron. Mater. 2019, 5, 1900134 .

[29] Samardak, A.S.; Davydenko, A.V.; Kolesnikov, A.G.; Samardak, A.Y.; Kozlov, A.G.; Pal, B.; Ognev, A.V.; Sadovnikov, A.V.; Nikitov, S.A.; Gerasimenko, A.V.; Cha, I.H. Enhancement of perpendicular magnetic anisotropy and Dzyaloshinskii-Moriya interaction in thin ferromagnetic films by atomic-scale modulation of interfaces. NPG Asia Mater. 2020, 12, 51.

[30] Fan, X.; Celik, H.; Wu, J.; Ni, C.; Lee, K.J.; Lorenz, V.O.; Xiao, J.Q. Quantifying interface and bulk contributions to spin–orbit torque in magnetic bilayers. Nat. Commun. 2014,5, 3042.

[31] Seung-heon, C.B.; Amin, V.P.; Oh, Y.W.; Go, G.; Lee, S.J.; Lee, G.H.; Kim, K.J.; Stiles, M.D.; Park, B.G.; Lee, K.J. Spin currents and spin–orbit torques in ferromagnetic trilayers. Nat. Mater. 2018, 17**,** 509.

[32] Fert, A.; Cros, V.; Sampaio, J. Skyrmions on the track. Nat. Nanotech. 2013, 8, 152.

[33] Ryu, K.S.; Thomas, L.; Yang, S.H.; Parkin, S. Chiral spin torque at magnetic domain walls. Nat. Nanotech. 2013, 8, 527.

[34] Hellman, F.; Hoffmann, A.; Tserkovnyak, Y.; Beach, G.S.; Fullerton, E.E.; Leighton, C.; MacDonald, A.H.; Ralph, D.C.; Arena, D.A.; Dürr, H.A.; Fischer, P. Interface-induced phenomena in magnetism. Rev. Mod. Phys. 2017, 89, 025006.

[35] Strempfer, J.; Francoual, S.; Reuther, D.; Shukla, D.K.; Skaugen, A.; Schulte-Schrepping, H.; Kracht, T.; Franz, H. Resonant scattering and diffraction beamline P09 at PETRA III. J. Synchrotron Rad. 2013, 20, 541.

[36] Gloskovskii, A.; Stryganyuk, G.; Fecher, G.H.; Felser, C.; Thiess, S.; Schulz-Ritter, H.; Drube, W.; Berner, G.; Sing, M.; Claessen, R.; Yamamoto, M. Magnetometry of buried layers-

Linear magnetic dichroism and spin detection in angular resolved hard X-ray photoelectron spectroscopy. J. Electron Spectrosc. Relat. Phenom. 2012, 185, 47.

[37] Parratt L. G. Surface Studies of Solids by Total Reflection of X-Rays. Phys. Rev. 1954, 95, 359.

[38] Bedzyk, M. J.; Bommarito, G. M.; Schildkraut, J. S. X-ray standing waves at reflecting mirror surface. Phys. Rev. Lett. 1989, 62, 1376. Bedzyk, M. J. "X-RAY STANDING WAVE AT THE TOTAL REFLECTION CONDITION" The X-ray Standing Wave Technique. World Scientific, 2013, 7, 94.

[39] Ghose, S.K.; Dev, B.N. X-ray standing wave and reflectometric characterization of multilayer structures. Phys. Rev. B, 2001, 63 (24), 245409.

[40] Graat, P.; Somers, M.A.J. Quantitative analysis of overlapping XPS peaks by spectrum reconstruction: determination of the thickness and composition of thin iron oxide films. Surf. Interface Anal. 1998, 26, 773 .

[41] Di Castro, V.; Ciampi, S. XPS study of the growth and reactivity of Fe/MnO thin-films. Surf. Sci. 1995, 294, 331.

[42] Yu, G.H.; Chai, C.L.; Zhu, F.W.; Xiao, J.M.; Lai, W.Y. Interface reaction of NiO/NiFe and its influence on magnetic properties. Appl. Phys. Lett. 2001, 78, 1706.

[43] Yamashita, T.; Hayes, P. Analysis of XPS spectra of Fe^{2+} and Fe^{3+} ions in oxide materials. Appl. Surf. Sci. 2008, 254, 2441.

[44] Grosvenor, A.P.; Kobe, B.A.; Biesinger, M.C.; McIntyre, N.S. Investigation of multiplet splitting of Fe 2p XPS spectra and bonding in iron compounds. Surf. Interface Anal. 2004, 36, 1564.

[45] Biesinger, M.C.; Payne, B.P.; Grosvenor, A.P.; Lau, L.W.; Gerson, A.R.; Smart, R.S.C. Resolving surface chemical states in XPS analysis of first row transition metals, oxides and hydroxides: Cr, Mn, Fe, Co and Ni. Appl. Surf. Sci. 2011, 257, 2717.

[46] Huttel, Y.; Navarro, E.; Telling, N.D.; Van der Laan, G.; Pigazo, F.; Palomares, F.J.; Quintana, C.; Roman, E.; Armelles, G.; Cebollada, A. Interface alloying effects in the magnetic properties of Fe nanoislands capped with different materials. Phys. Rev. B 2008, 78**,** 104403.

[47] Powell, C.J.; Tanuma S. Hard X-ray Photoelectron Spectroscopy (HAXPES). Springer, Switzerland, 2016, 59, 111.

[48] Chastain, J.; King Jr, R.C. Handbook of X-ray photoelectron spectroscopy. Perkin-Elmer Corporation, 1992, 40, 221.

[49] You, C.Y.; Fu, H.R.; Zhang, X.; Tian, N.; Wang, P.W. Interaction of Ta–O and perpendicular magnetic anisotropy of Ta/Pd (0–2.4 nm)/$Co_2FeAl_{0.5}Si_{0.5}$/MgO/Ta structured films. J. Magn. Magn. Mater. 2015, 377, 276.

[50] Vaz, C.A.F.; Prabhakaran, D.; Altman, E.I.; Henrich, V.E. Experimental study of the interfacial cobalt oxide in Co_3O_4/αAl_2O_3 (0001) epitaxial films. Phys. Rev. B 2009, 80, 155457.

[51] Bardi, U.; Beard, B.; Ross, P. N. Co chemisorption on the [111] and [100] oriented single crystal surfaces of the alloy $CoPt_3$. J. Catal. 1990, 124, 22.

[52] Martinez, G.; Malumbres, A.; Lopez, A.; Mallada, R.; Hueso, J.L.; Santamaria, J. Laser-assisted production of carbon-encapsulated Pt-Co alloy nanoparticles for preferential oxidation of carbon monoxide. Front. Chem. 2018, 6, 487 .

[53] Demchenko, I.N.; Syryanyy, Y.; Melikhov, Y.; Nittler, L.; Gladczuk, L.; Lasek, K.; Cozzarini, L.; Dalmiglio, M.; Goldoni, A.; Konstantynov, P.; Chernyshova, M. X-ray

photoelectron spectroscopy analysis as a tool to assess factors influencing magnetic anisotropy type in Co/MgO system with gold interlayer. Scripta Materialia 2018, 145, 50.

[54] Wen, Z.; Hadorn, J.P.; Okabayashi, J.; Sukegawa, H.; Ohkubo, T.; Inomata, K.; Mitani, S.; Hono, K. Interdiffusion in epitaxial ultrathin Co2FeAl/MgO heterostructures with interface-induced perpendicular magnetic anisotropy. Appl. Phys. Express 2017, 10, 013003 .

TABLE I. Results from the fitting of x-ray reflectivity of the complete multilayer sample. Typical error bars in the determination of the thicknesses and roughnesses of different layers are ± 0.1

Layer	Thickness (nm)	Roughness (nm)
Ta	1.4	0.3
MgO	0.7	0.6
CFA	2.0	0.2
Ta	7.0	0.5
MgO	3.3	0.5
Si	4.1	0.6
Mo	2.6	0.4

TABLE II. Fitting parameters of Fe $2p_{3/2}$ and Co $2p_{3/2}$ HAXPES spectra of the sample in pristine state.

Element	Angle (°)	CFA		CFA-Ta		CFA-O					
		Position (eV)	Area (%)	Position (eV)	Area (%)	Position (eV)	Area (%)	Position (eV)	Area (%)	Position (eV)	Area (%)
Fe	0.63	707	42	707.9	23	709	5	710	19	711.3	11
	0.73	707	46	707.9	31	709	8	710	11	711.3	4
	0.82	707	49	707.9	33	709	7	710	9	711.3	2
	1.02	707	44	707.9	24	709	7	710	13	711.3	12
Co	0.63	778.3	54	779	25	779.6	7	780.5	14		
	0.73	778.3	52	779	29	779.6	5	780.5	14		
	0.82	778.3	49	779	31	779.6	3	780.5	17		
	1.02	778.3	52	779	26	779.6	6	780.5	16		

TABLE III. Fitting parameters of Fe $2p_{3/2}$ and Co $2p_{3/2}$ HAXPES spectra of the sample after annealing at 200℃ for 1h.

Element	Angle (°)	CFA		CFA-Ta		CFA-O					
		Position (eV)	Area (%)	Position (eV)	Area (%)	Position (eV)	Area (%)	Position (eV)	Area (%)	Position (eV)	Area (%)
Fe	0.63	707	39	707.9	24	709	6	710	20	711.3	11
	0.73	707	44	707.9	27	709	7	710	15	711.3	7
	0.82	707	45	707.9	28	709	7	710	13	711.3	7
	1.02	707	36	707.9	22	709	5	710	23	711.3	14
Co	0.63	778.4	60	779.1	27	779.7	4	780.6	9		
	0.73	778.4	60	779.1	27	779.7	4	780.6	9		
	0.82	778.4	62	779.1	26	779.7	4	780.6	8		
	1.02	778.4	58	779.1	26	779.7	5	780.6	11		

FIGURE CAPTIONS

Figure 1. Schematic diagram of the sample structure.

Figure 2. X- ray reflectivity of a) Mo/Si multilayer before the deposition of the structure to be studied, b) MgO/Ta/CFA/MgO/Ta deposited on the Si substrate, and c) the complete sample structure. The continuous curves represent the best fit to experimental data.

Figure 3. a**)** Contour plot of the x-ray intensity as a function of depth and the grazing angle of incidence α of x-rays with respect to the sample surface. Darker shade represents higher intensity. Hatched area represents the position of Co_2FeAl layer. The four angles of incidence at which HAXPES measurements have been done are marked by horizontal lines. b**)** Variation in the intensity of the x-rays as a function of depth for the four angles of incidence at which HAXPES measurements are done. One may note that, α = 0.63° and 1.02° correspond to a situation in which the top interface has a higher x-ray intensity as compared to the bottom interface, while for α = 0.82° the situation is reverse. For α = 0.73°, x-ray intensity is almost uniform across the CFA layer

Figure 4. Fe $2p_{3/2}$ HAXPES spectra of pristine sample taken at different grazing angles of incidence α, with best fitting of experimental data.

Figure 5. Relative intensities of the oxide, metallic Fe and Fe-Ta alloy components corresponding to different angles of incidence in HAXPES spectra of Fe $2p_{3/2}$.

Figure 6. Co $2p_{3/2}$ HAXPES spectra of pristine sample taken at different grazing angles of incidence (α) with best fitting of experimental data.

Figure 7. Relative intensities of the oxide, metallic Co and Co-Ta alloy components corresponding to different angles of incidence in XPS spectra of Co $2p_{3/2}$.

Figure 8. Fe $2p_{3/2}$ HAXPES spectra of the sample annealed at 200℃, taken at different grazing angles of incidence (α), with best fitting of experimental data.

Figure 9. Co $2p_{3/2}$ HAXPES spectra of the sample annealed at 200℃, taken at different grazing angles of incidence (α), with best fitting of experimental data.

Figure 10. Relative intensities of the oxide, metallic Fe and Fe-Ta alloy components corresponding to different angles of incidence in XPS spectra of Fe $2p_{3/2}$ after annealing.

Figure 11. Relative intensities of the oxide, metallic Co and Co-Ta alloy components corresponding to different angles of incidence in XPS spectra of Co $2p_{3/2}$ after annealing.

Figure 1.

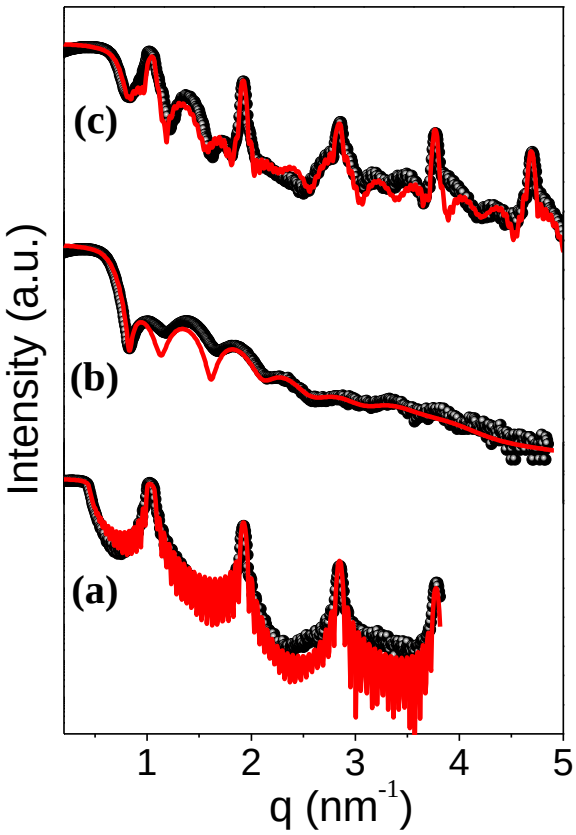

Figure 2.

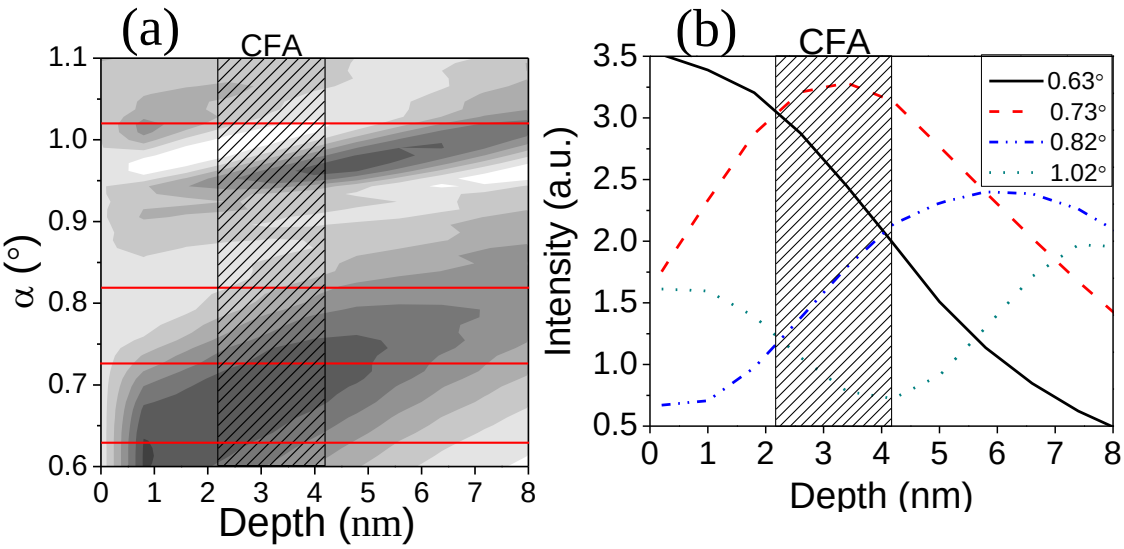

Figure 3.

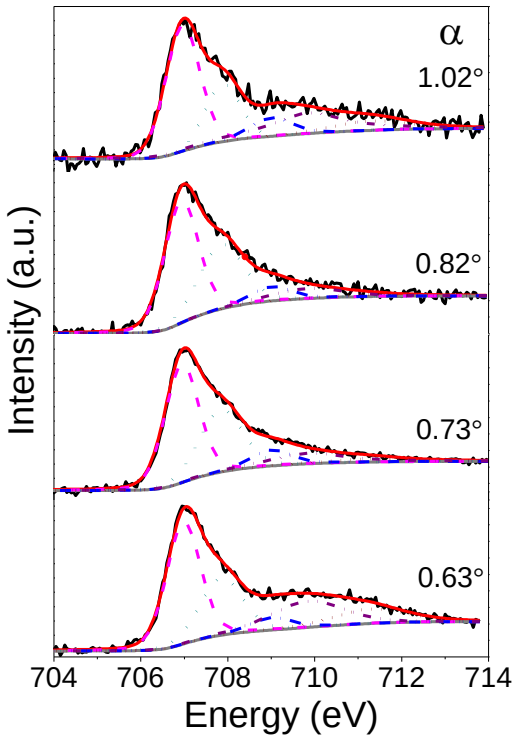
α
1.02°
0.82°
0.73°
0.63°
Intensity (a.u.)
704
706
708
710
712
714
Energy (eV)

Figure 4.

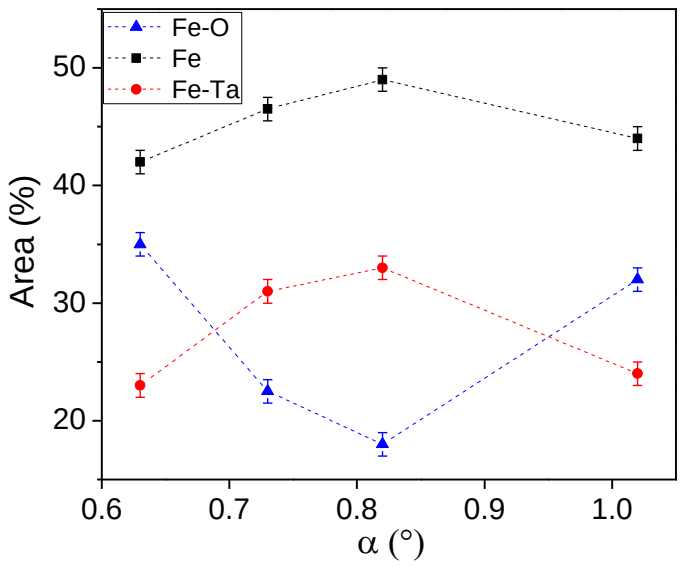

Figure 5.

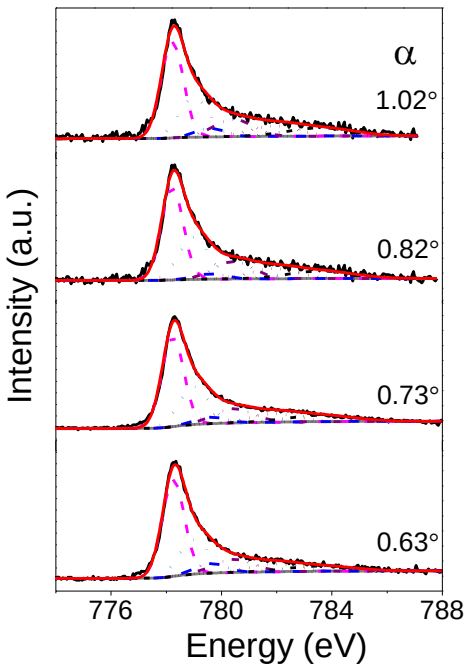

Figure 6.

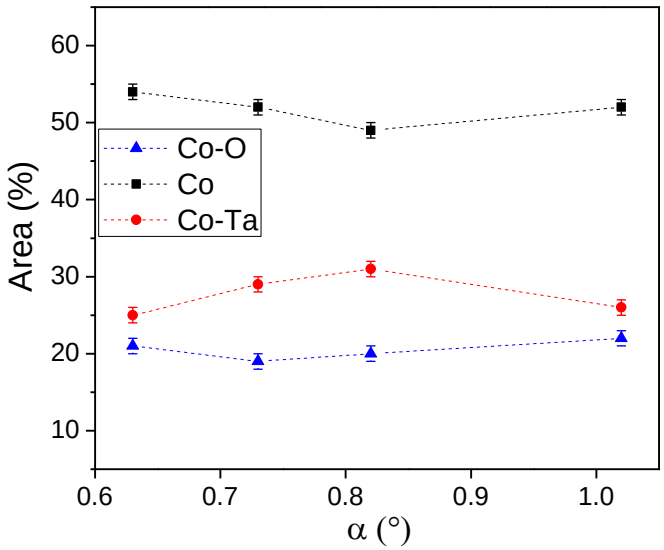

Figure 7.

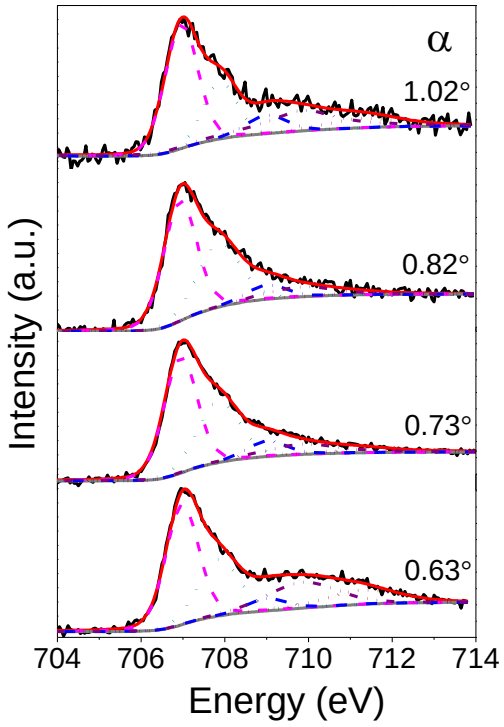
α
1.02°
0.82°
0.73°
0.63°
Intensity (a.u.)
704
706
708
710
712
714
Energy (eV)

Figure 8.

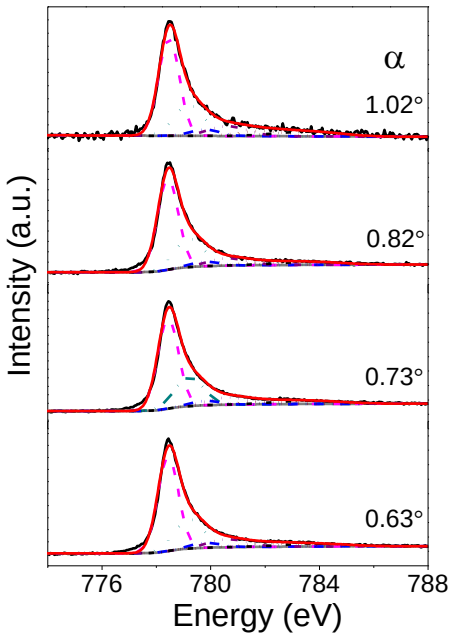

Figure 9.

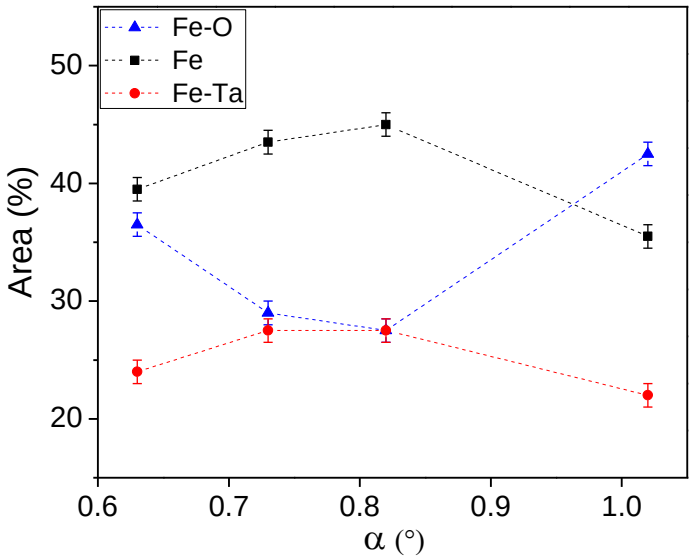

Figure 10.

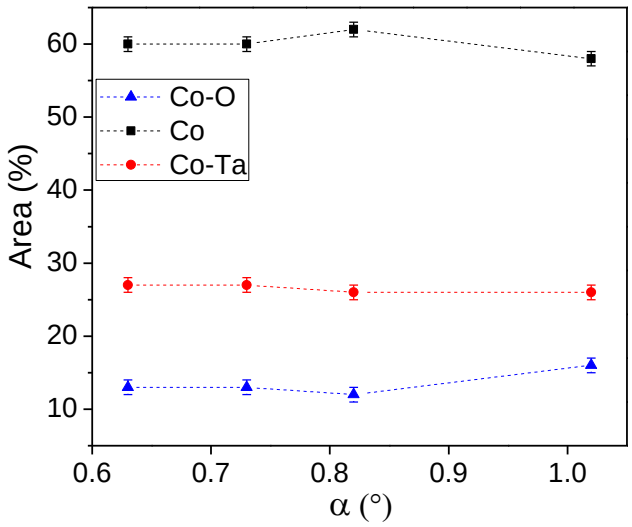

Figure 11.